Dynamic vs. quasi-static shear failure of high strength metallic alloys: Experimental issues

Patrice Longère, André Dragon

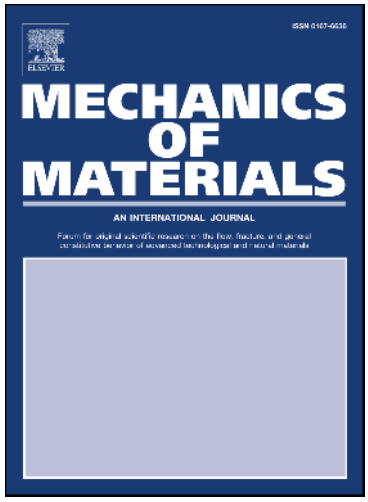

Dynamic vs. quasi-static shear failure of high strength metallic alloys: Experimental issues

Patrice Longère, André Dragon

PII: S0167-6636(14)00095-7
DOI: http://dx.doi.org/10.1016/j.mechmat.2014.05.001
Reference: MECMAT 2273

To appear in: *Mechanics of Materials*

Received Date: 18 October 2013
Revised Date: 31 March 2014

Please cite this article as: Longère, P., Dragon, A., Dynamic vs. quasi-static shear failure of high strength metallic alloys: Experimental issues, *Mechanics of Materials* (2014), doi: http://dx.doi.org/10.1016/j.mechmat.2014.05.001

Dynamic vs. quasi-static shear failure of high strength metallic alloys: Experimental issues

Patrice Longère[11], and André Dragon[2]

[1] Université de Toulouse
Institut Supérieur de l'Aéronautique et de l'Espace (ISAE) - Institut Clément Ader (EA 814)
10 avenue E. Belin, BP 54032, 31055 Toulouse cedex 4, France
e-mail: patrice.longere@isae.fr

[2] CNRS-Institut Pprime (UPR 3346)
ISAE / Ecole Nationale Supérieure de Mécanique et d'Aérotechnique - Université de Poitiers
1 avenue C. Ader, BP 40109, 86961 Futuroscope - Chasseneuil du Poitou, France
e-mail: andre.dragon@ensma.fr

ABSTRACT

Ductile fracture of metals by void nucleation, growth and coalescence under positive stress triaxiality is well admitted. This is not the case when metals are submitted to negative stress triaxiality. The present work aims at contributing to a better understanding of the competition between micro-mechanisms at the origin of failure of metals when submitted to shear-pressure loading at low and high strain rates. With this aim in view, experiments were carried out on Ti-6Al-4V shear-compression samples involving a stress triaxiality range comprised between -0.2 and -0.5. Results show that the material failure is the consequence of a void growth induced process. At high strain rate, due to the localization of the deformation within adiabatic shear bands, the failure of the material occurs earlier, leading to maximum shear strain smaller at high strain rate than at low strain rate. Impact tests were also carried out on Kalthoff and Winkler type double notched plates. They showed that the interaction between tension and shear waves leads to a complex Mode I-Mode II crack propagation.

Keywords: Ti-6Al-4V – Shear failure – Dynamic fracture – Adiabatic shear banding – Microstructure

1. Introduction

In engineering applications, structures are generally submitted to complex loading paths. Predicting the conditions for their potential catastrophic failure consequently requires the knowledge of the dependence of the material ductility on the loading parameters, including notably the loading magnitude, the loading rate, the temperature, etc. In view of incorporating the influence of all these parameters (and others) within a failure criterion, or

[1] Corresponding author.
E-mail address: patrice.longere@isae.fr (P. Longère).

better within a constitutive model, the microscopic mechanisms governing the ductility of the materials at stake have to be investigated previously.

Whereas the metal fracture under positive stress triaxiality is quite well understood – resulting mostly from void germination, growth and coalescence, see e.g. Hancock and Mackenzie (1976) and Goods and Brown (1979) –, there remain gaps to fill in the comprehension (and description) of metal failure under low (near zero) and negative stress triaxialities.

At low strain rate, studies available in literature mostly focus on determining the macroscopic conditions for failure of metals under combined shear-tension loading, with the development of specific sample geometries and/or experimental devices, see e.g. Osakada et al. (1977), Manach and Favier (1997), Mohr and Oswald (2008), Driemeier et al. (2010). Macroscopic failure criteria are accordingly proposed, accountig for the effect of stress triaxiality, strain rate and temperature, see e.g. Johnson and Cook (1985), or of stress triaxiality and Lode parameter, see e.g. Bao and Wierzbicki (2004), Barsoum and Faleskog (2007), Coppola et al. (2009), Papasidero et al. (2013). In parallel, scarce are the experimental investigations aiming at identifying the micromechanims at the origin of shear failure. Under zero and low negative triaxiality, the failure is mostly ascribed to micro-shear decohesion, see Bao and Wierzbicki (2004) and Brünig et al. (2011), whereas it has been observed to result from micro-void growth by Longère and Dragon (2013).

Comparatively, literature dedicated to shear failure investigation at high strain rate is paradoxically much more abundant, in particular when dealing with the dynamic shear localisation phenomenon known as adiabatic shear banding (ASB), see e.g. Bai and Dodd (1992) for a description of the phenomenon. Possibly, in order to optimize the ballistic properties of high strength metals and alloys, ASB-related studies often include microstructural aspects. For example, ASB in high strength metallic materials has been investigated in high strain rate torsion by Marchand and Duffy (1988) and Bai et al. (1994), punching by Mazeau et al. (1997), combined shear-compression by Beatty et al. (1992), Longère et al. (2005), and Vural et al. (2003), this list being far from being exhaustive.

The present work aims at contributing to a better understanding of the competition between micro-mechanisms at the origin of failure of metals when submitted to overall shear-pressure loading at low and high strain rates. Shear-pressure loading involving negative stress triaxiality is encountered in many engineering problems including notably metal cutting and thick plate impact. As the strain rate may significantly vary all along the loading duration, its influence on shear failure is herein particularly investigated.

Due to their low mass density and high resistance, Titanium alloys are nowadays widely used as structural materials in many industrial sectors, such as aeronautics and defense. The material under consideration in the present work is the Ti-6Al-4V ELI Titanium alloy.

This experimental investigation is split in two parts.

The first part (Section 2) is devoted to the identification of the micro-mechanisms leading to shear failure at low and moderate strain rates. Experiments were carried out with hat shape samples (HSS), as designed by Meyer and Manwaring (1986) and Couque (2003), respectively, and shear-compression specimens (SCS), as designed by Rittel et al. (2002). The stress triaxiality values involved in the samples are negative, ranging typically from -0.2

to -0.5 depending on the specimen considered. Low strain rate shear-pressure tests were performed using a conventional tension/compression testing machine and high strain rate ones employing split Hopkinson pressure bar (SHPB). In order to identify the current and ultimate material degradation states, some tests were (if possible) interrupted before failure and other ones were carried out until complete fracture. In parallel, in view of evaluating the possibility of obtaining shear stress-shear strain curves from tests using these three sample geometries, a calibration was conducted via finite element numerical simulation.
At low strain rate, involving quasi isothermal conditions, the material failure has been seen to result from void growth and further dimple formation, in spite of the overall pressure applied. At high strain rate, involving quasi adiabatic conditions, the material failure has been found to result from the adiabatic shear banding (ASB) localisation mechanism, as expected for this class of alloys, followed by void growth along the band.

The second part (Section 3) deals with Kalthoff and Winkler (KW) impact test, see Kalthoff and Winkler (1987), carried out in view of evaluating the dynamic crack arrest ability of double notched structures. In some cases, this test and its single notched structure variant, as proposed by Zhou, Rosakis and Ravichandran (ZRR), see Zhou et al. (1996) and Kalthoff and Bürgel (2004), allow to identify a critical impact velocity, associated to a dynamic 'brittle-ductile' failure mode transition. The 'brittle-ductile' failure mode transition velocity is the velocity below which the crack propagation operates in (opening) Mode I at a significant angle (around +70°) wrt the notch and beyond which the crack propagation operates in (ASB-assisted slip) Mode II at a negligible (slightly negative) angle wrt to the notch. This definition of 'brittle-ductile' transition velocity may slightly vary depending on the aforementioned authors. Unlike the works quoted previously, impact tests performed in the present study on Ti-6Al-4V double notched (KW) plates have shown that at low impact velocity the crack propagates at a negligible (slightly negative) angle wrt the notch, and that at higher impact velocity the crack, which has firstly propagated at a negligible (slightly negative) angle wrt the notch, propagates at a significant (positive) angle wrt the notch. Microscopic observation of the fracture surface moreover shows no evidence of ASB but the presence of dimples whose shape indicates a complex loading path.

Finally, relying upon the experimental results obtained in the present work, concluding remarks propose a list of indications in view of elaborating a constitutive model aiming at reproducing the shear failure of metallic materials when submitted to a wide range of strain rates.

2. Shear failure at low and moderate loading rates

As mentioned in the introduction, literature on shear-compression experiments at low strain rate is scarce while being paradoxically rich at high strain train rate. In the sequel, we are using different specimen geometries initially proposed by different authors to study the dynamic shear behaviour of high strength materials.
The core of the present work is devoted to the identification of the damage mechanisms operating at low and high strain rates, which is the purpose of subsection 2.3, in view of further constitutive modelling (not presented here). Subsection 2.2 is accordingly considered as a complement attempting to give (more qualitative than quantitative) information on the shear-pressure behaviour of the material at stake.

2.1. Experimental procedure

Shear-compression tests were carried out at room temperature at low and moderate strain rates using conventional hydraulic tension/compression testing machine and split Hopkinson pressure bar (SHPB), respectively. They consist in loading hat shape samples (HSS), as designed by Meyer and Manwaring (1986) and Couque (2003), respectively, and shear-compression specimens (SCS), as designed by Rittel et al. (2002), see Fig.1. These samples are dimensioned to allow for generating a local shear loading under a global compression loading. It must be noted that some other variants of hat-shaped specimens have been employed for controlled adiabatic shear banding. For instance, the configuration by Beatty has been subjected to thorough ASB investigation including numerical simulations, see Nemat-Nasser et al. (1994).

In the sequel, HSS-MM stands for Meyer-Manwaring-type hat-shaped sample, HSS-C for Couque-type hat-shaped sample, and SCS-RLR for Rittel-Lee-Ravichandran-type shear-compression specimens, in reference to the foregoing works. Specimen dimensions used in the present study are specified in Fig.1.

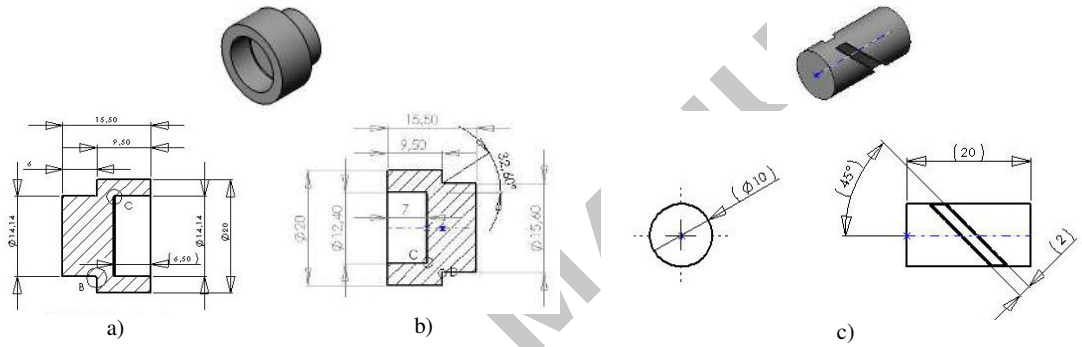

Fig.1: Schematic representation of the shear test specimens used in the present work.
a) HSS-MM geometry ; b) HSS-C geometry ; c) SCS-RLR geometry

In a first step, numerical simulations were conducted to determine values of stress triaxiality ST (defined as the ratio of the mean stress σ_{mean} over the Mises equivalent stress σ_{eq}, i.e. $ST = \sigma_{mean} / \sigma_{eq}$) in some elements of the sheared zone of specimens represented in Fig.1. With this aim in view, the engineering finite element computation code Abaqus was employed. Every meshed sample is represented in Fig.2, considering axisymmetric finite elements for HSS-MM and HSS-C configurations and three-dimensional finite elements for SCS-RLR configuration (with plane symmetry allowing to mesh half the specimen), with fine meshing in the sheared zone. The material behaviour was derived from compression tests (not shown here) carried out on the same material. For low strain rate configurations numerically simulated using implicit time integration scheme, the material behaviour considered is drawn in Fig.3; for high strain rate configurations numerically simulated using explicit time integration scheme, strain rate and temperature effects were accounted for via Johnson-Cook model, see Johnson and Cook (1983), with A=739MPa, B=906MPa, n=0.314, C=0.0072, m=0.67, $\dot{\varepsilon}_{ref}=10^{-3}s^{-1}$, T_{ref}=293K, T_{melt}=1700K, and inelastic heat fraction β=1. On the other hand, neither damage nor failure was taken into account in the numerical simulations.

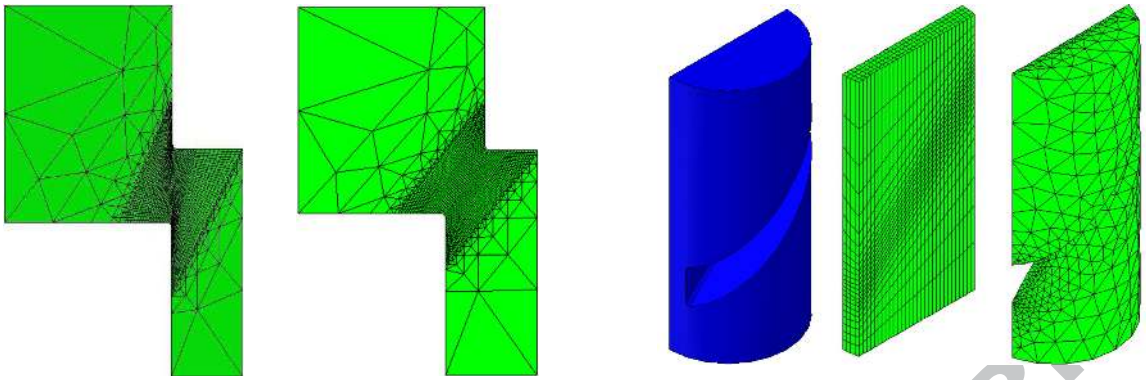

a) HSS-MM b) HSS-C c) SCS-RLR

Fig.2: Finite element discretization of a) HSS-MM, b) HSS-C and c) SCS-RLR used in numerical simulation (Abaqus).

In Fig.4 evolution of computed local stress triaxiality ST values is reported as a function of the local shear strain γ, from the beginning of plastic deformation, for the three sample geometries, in a finite element located near the middle of the intense shear zone, during a low strain rate loading. One can accordingly notice that the stress triaxiality tends to a value close to -0.2 for HSS-MM and SCS-RLR, while beginning with a value of -0.15 for the former and -0.3 for the latter, and close to -0.5 for HSS-C, with a slight evolution along the loading. During the (real) process of damage leading to ultimate fracture, stress triaxiality in the sheared zone is expected to evolve and possibly take values (very) different from those obtained in the present numerical simulations.

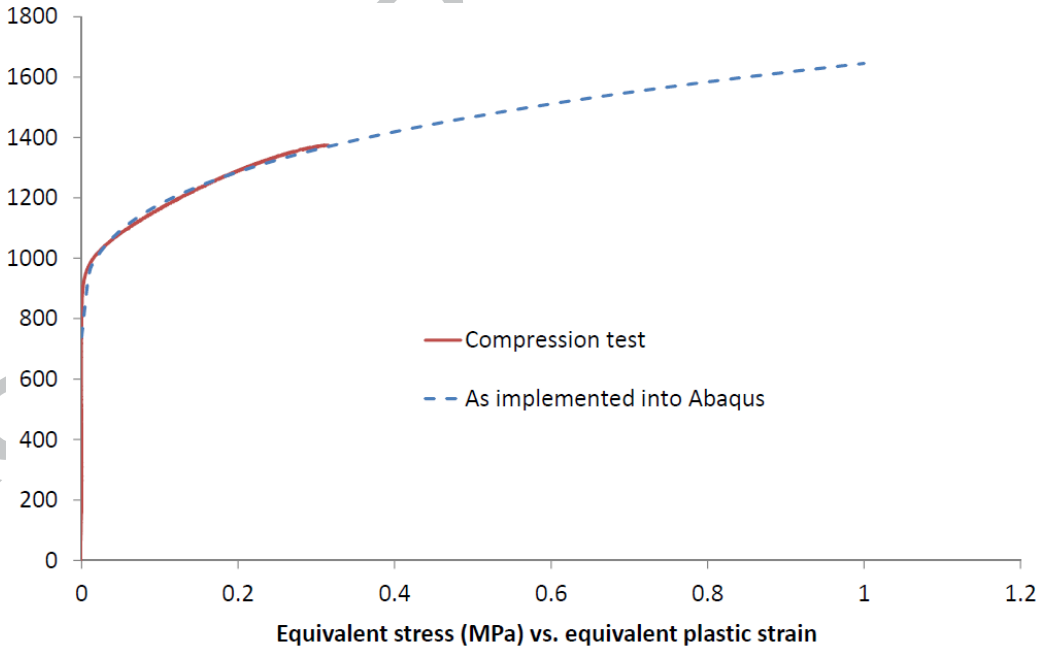

Fig.3: Material behaviour as obtained from quasi-static compression tests and used for the numerical simulations for low strain rate configurations - Ti-6Al-4V.

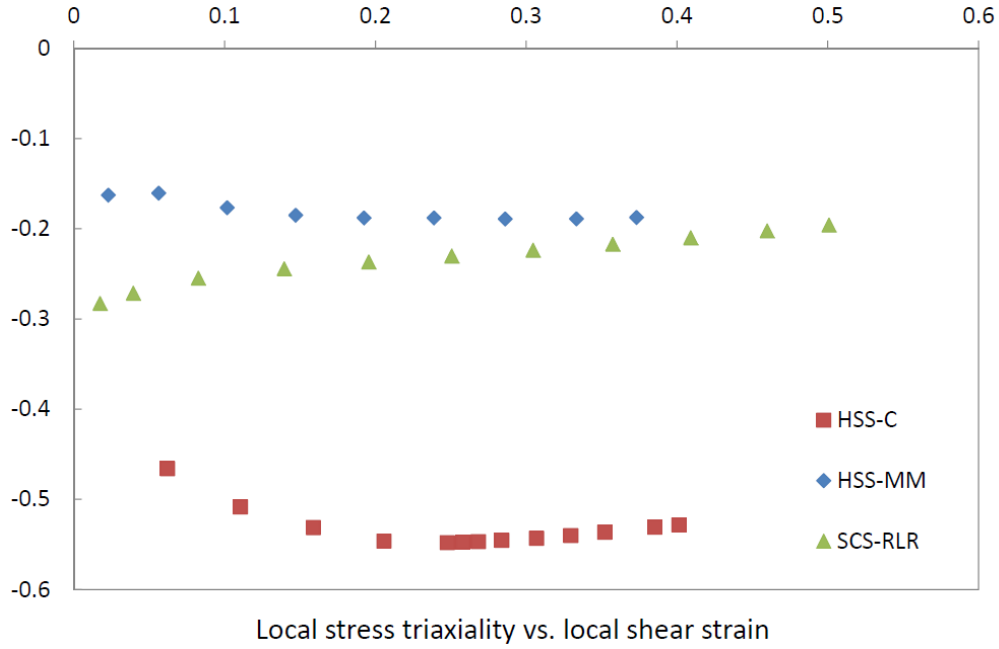

Fig.4: Local stress triaxiality vs. local shear strain for the three sample geometries. Results from numerical simulations considering low strain rate loading - Ti-6Al-4V.

2.2. Shear stress-shear strain curves

The specimens whose geometries are given in Fig.1 were designed by their authors to favour shear loading in a controlled zone, in view for some of them of studying the adiabatic shear banding susceptibility of metals and alloys. According to this point, we are here considering the experiments using the specimens in question as shear tests under pressure. The stress-strain curves given below are accordingly related to shear. Numerical simulations outlined in the previous subsection permit estimating relations between global specimen crushing ΔL and local (inside the sheared zone) shear strain γ on the one hand, and between applied load F and shear stress τ on the other. The global shear strain Γ, resp. shear stress T, is deduced from the relative displacement ΔL of the upper and lower specimen sides, resp. load F, according to

$$\Gamma = \frac{\Delta L}{w_{shear}} \; ; \; T = \frac{F}{S_{shear}} \qquad (1)$$

where w_{shear} and S_{shear} represent the width and section area of the sheared zone, respectively, see Table 2. The local shear strain γ and stress τ are determined via

$$\gamma = \varepsilon_{\max} - \varepsilon_{\min} \; ; \; \tau = 0.5(\sigma_{\max} - \sigma_{\min}) \qquad (2)$$

where $\varepsilon_{\min}$, $\varepsilon_{\max}$, $\sigma_{\min}$ and $\sigma_{\max}$ represent the minimal and maximal, strain and stress, respectively, as extracted from finite element located inside the sheared zone. Comparing the global and local, numerical values of strain and stress yields

$$\gamma = \alpha_\gamma \Gamma \; ; \; \tau = \alpha_\tau T \qquad (3)$$

Values of fitting coefficients α_γ and α_τ, which are specific to the material considered (Ti-6Al-4V in the present case), in (3) have been seen to keep a constant value for quasi-static loading ($21\text{x}10^{-3}$ and 1 for HSS-MM specimen; $25\text{x}10^{-3}$ and 1 for HSS-C specimen; 1 and 1 for SCS-RLR specimen), and to evolve during the deformation process for dynamic loading. Finally, the plastic shear strain γ^p was deduced from

$$\gamma^p = \gamma - \gamma^e = \gamma - \frac{\tau}{\mu} \tag{4}$$

where γ and γ^e represent the local, total and elastic shear strains, and μ the shear elasticity modulus.

Experimentally, the overall relative displacement ΔL and load F were measured using a mechanical extensometer and the load sensor of the testing machine for quasi-static tests and strains of input and output bars of the split Hopkinson pressure bar device for dynamic tests, see e.g. Rittel et al. (2002). Experimental local shear stress-shear strain curves obtained at low (10^{-3}-10^{-2} s^{-1}) and high (10^{2}-10^{3} s^{-1}) shear strain rates and at room temperature are drawn in Figs.5-7 for the tests carried out on HSS-MM, HSS-C and SCS-RLR, respectively. According to Figs.5 and 7, the material is subject to a nonlinear strain hardening for shear strains lower than 0.05 and to a quasi linear strain hardening for shear strains greater than 0.05. Fig.6 shows a nonlinear strain hardening all along the shear stress-shear strain curve.

According to Figs.5-7 and as expected for Titanium alloys, one can observe that the higher the strain rate the higher the resistance (in shear) of the material. One can also notice that the higher the strain rate, the smaller the shear strain at failure – except for the case of the HSS-C test which did not lead to fracture at high strain rate –, as the result of a change in the micro-mechanisms governing the material failure between low and high strain rate.

Shear stress-shear strain curves obtained with the three specimen geometries are superposed in Fig.8. One can note that the curves group by strain rate magnitudes, i.e. low and high strain rates, even though there are some discrepancies within a given group. In absence of a larger number of stress triaxiality values, it is difficult to draw a rule on the influence of the stress triaxiality on the shear strain at failure. Fig.8 seems however to show that, at least at low strain rate, the higher the pressure, or equivalently the higher (in absolute value) the stress triaxiality, see Fig.4, the larger the shear strain at failure. The latter result is qualitatively in agreement with the trend observed by Bao and Wierzbicki (2004) in the negative stress triaxiality range while seemingly pushing away the asymptote they fix at a stress triaxiality value of -1/3 for material damage and further failure – experiments using HSS-C indeed involve an averaged stress triaxiality value close to -0.5, see Fig.4.

These results should be looked upon as indicative markers rather than as quantitative ones.

Table 1: Notations for the shear test treatment – Ti-6Al-4V

	HSS-MM	HSS-C	SCS-RLR
w_{shear}	$\frac{D-d}{2}$	0.02mm	$\frac{\sqrt{2}w}{k_3}$
S_{shear} =	$\pi\frac{D+d}{2}H$	$\frac{\pi}{\cos\alpha}\frac{D+d}{2}\sqrt{\left(\frac{D-d}{2}\right)^2+H^2}$	$\frac{Dt}{k_1(1-k_2\gamma)}$

In Table 1 D et d represent the outer and inner diameters (see Fig.1), respectively, H the sheared zone height, t the sheared zone thickness (t=2mm), $\tan\alpha = \frac{D-d}{2H}$, k_1 = 0.50, k_2 = 0.12 and k_3 = 1.50.

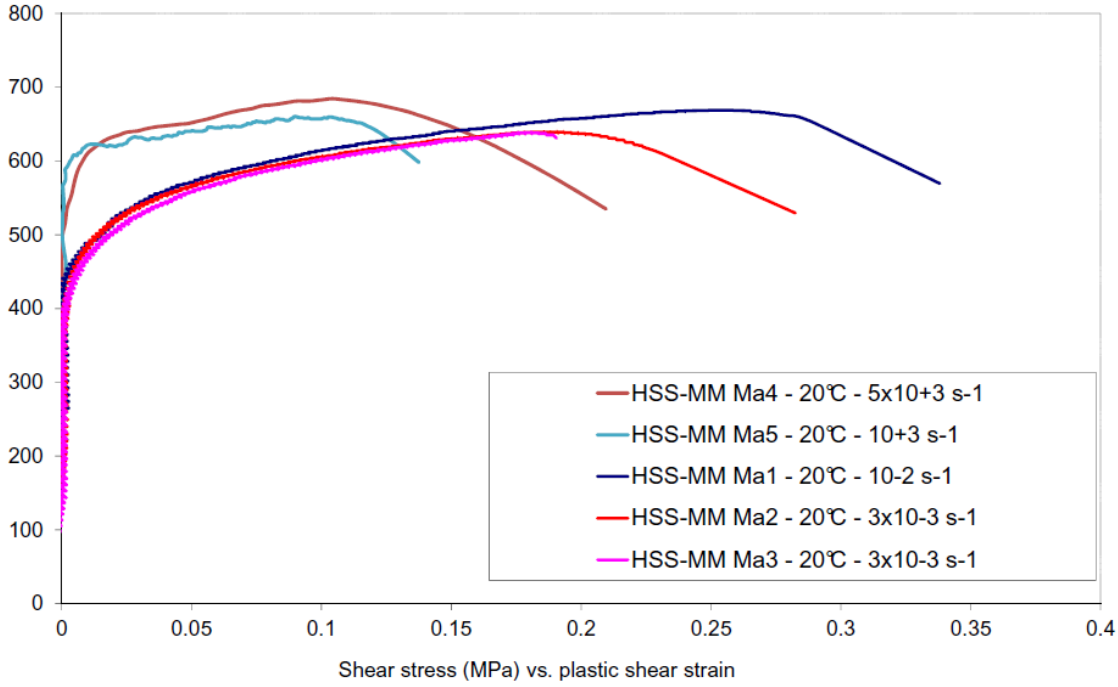

Fig.5: Local shear stress-shear strain curves obtained at room temperature at low and moderate strain rates using HSS-MM – Ti-6Al-4V
Ma1, Ma2 and Ma5 were carried out until failure ; Ma3 and Ma4 were interrupted before failure

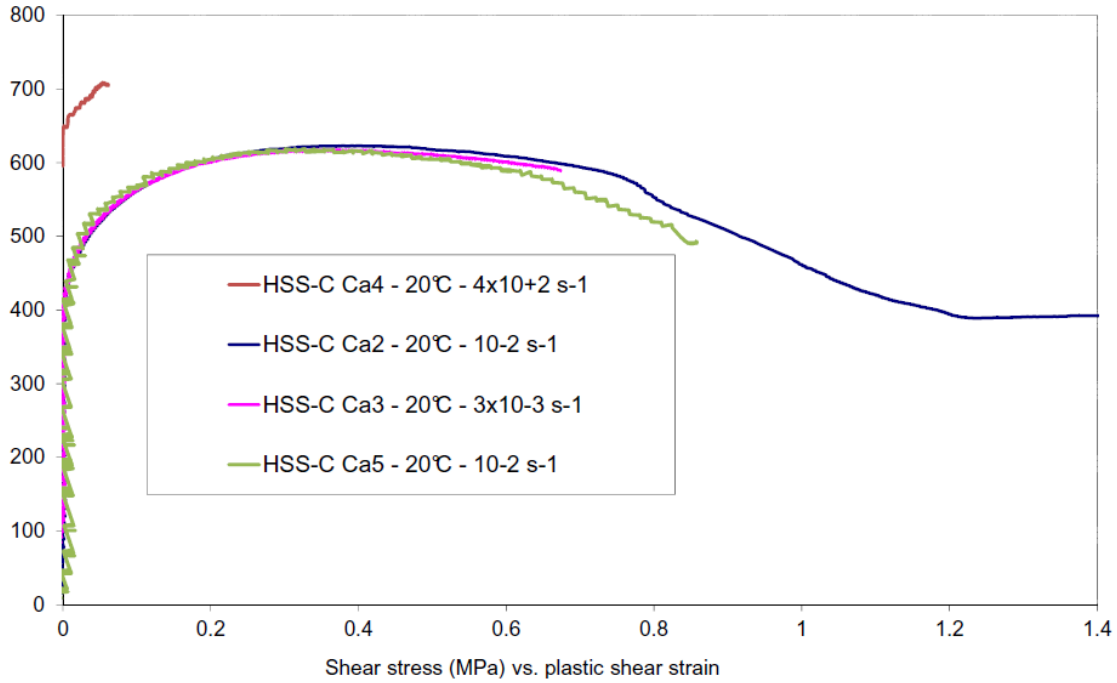

Fig.6: Local shear stress-shear strain curves obtained at room temperature at low and moderate strain rates using HSS-C – Ti-6Al-4V
Ca2 and Ca5 were carried out until failure ; Ca3 was interrupted before failure and Ca4 does not lead to fracture (low energy loading)

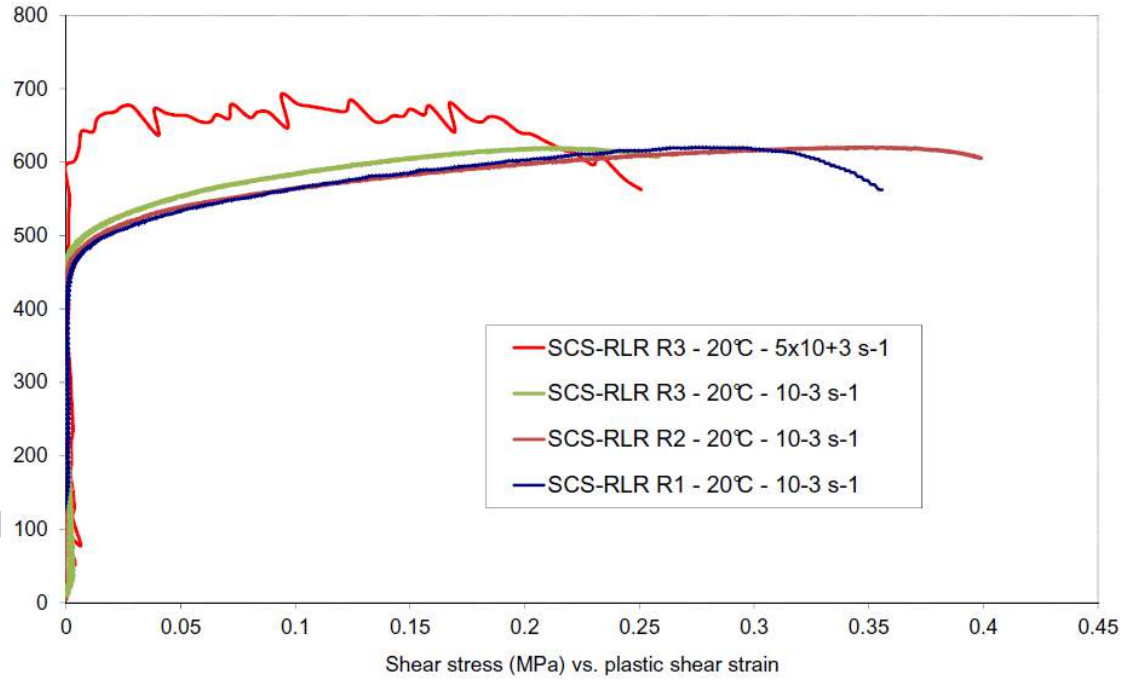

Fig.7: Local shear stress-shear strain curves obtained at room temperature at low and moderate strain rates using SCS-RLR – Ti-6Al-4V
R1, R2 and R3 dynamic were carried out until failure ; R3 static was interrupted before failure

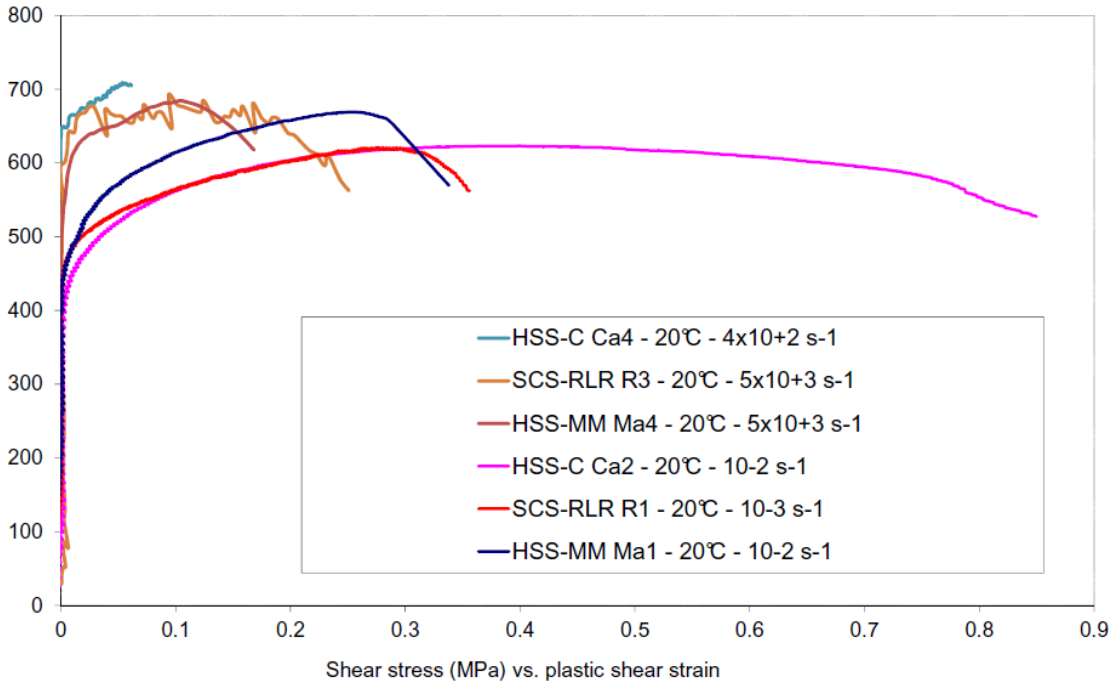

Fig.8: Superposition of local shear stress-shear strain curves obtained at room temperature at low and moderate strain rates using HSS-MM, HSS-C and SCS-RLR – Ti-6Al-4V

2.3. Fracture investigation

In view of identifying the current and ultimate material degradation states, some tests were (when it was possible) interrupted before failure and other ones were carried out until complete fracture.
Specimens submitted to interrupted loading were cut and polished. In the following, microscopic observations were carried out using scanning electron microscopy (SEM) on samples, first without reagent in order to identify the crack path then with Kroll's reagent in order to determine the micro-mechanisms of damage. The initial microstructure is characterized by the presence of hcp α grains and acicular α' (solute-lean, hcp) martensite in a bcc β matrix, also known as α + transformed β microstructure.

2.3.1. Low strain rate

Fig. 9 shows a crack which has partially propagated inside a HSS-MM submitted to interrupted loading. Two fracture ring-shaped planes were seen to initiate from the female and male parts of the specimen, see Fig.9a. Figs.9a-b show a quasi-continuous macro-crack with a trend of becoming more and more sinuous when it goes deeper inside the specimen, see also Fig.9.c. One can observe in Figs.9.d-e the presence of voids in the phase of coalescence by localised micro-shearing near the crack tip, see also Longère and Dragon (2013).
In configurations leading to complete failure, see Fig.10, fracture is characterized by the presence on the fracture surface of dimple clusters surrounded by as-buttered, flat surfaces, see in particular Fig.10.a. The presence of inclusion-containing dimples, as shown in Fig.10.b, demonstrates that the damage process is accompanied by dilatancy. These

microscopic observations allow concluding that void growth is the micro-mechanism of damage and failure of Ti-6Al-4V when submitted to shear-pressure loading, see also Longère and Dragon (2013).

Fig. 11 shows a crack which has partially propagated inside a HSS-C submitted to interrupted loading. Two fracture truncated cone-shaped planes were seen to initiate from the female and male parts of the specimen, see Fig.11a. The blunt front of the macro-crack in Figs.11.a-b (visible after adequate magnification) constitutes another evidence of ductile damage of the material at stake when submitted to shear-pressure loading. The crack propagation path is in this case straight, see also Fig.11.c., while being discontinuous, see Fig.11.d. One can also note from Fig.11.d. a strong reorientation of the α' martensite needles in the direction of shearing.

For the HSS-C configurations leading to complete failure, a coarse zoom shows only flat, void containing- and serrated edge-fracture surfaces, see Fig.12.a. At a finer scale, see Fig.12.b., one can distinguish the tracks of elongated dimples between the surfaces in question.

Fig. 13 shows a macroscopic view of a SCS-RLR after a test interrupted before fracture. In this test, it is expected that the shearing process operates inside the specimen part delimitated by the machined grooves, i.e. in the bulk part inclined at an angle of 45° wrt to the cylinder axis, see Fig.1.c. Figs.13.a-b show that a crack has partially propagated through the thickness of the specimen gauge, at an angle of about (slightly greater than) 45° wrt the specimen gauge side. The shear failure of a SCS-RLR is thus ideally the result of a crack contained in a rectangular surface whose length is collinear with the groove direction (45° wrt cylinder axis) and whose width located inside the specimen gauge thickness is inclined at an angle of 45° wrt the groove back.
The fracture surface of the specimen gauge after a test on a SCS-RLR until complete failure is shown in Fig.14. As for the HSS-MM and HSS-C, one can observe the presence of clusters of very small elongated dimples surrounded by flat surfaces, as the result of void growth induced damage.

2.3.2. Moderate strain rate

Fig.15 shows a ring-shaped adiabatic shear band in a HSS-MM after interrupted test as the result of the meeting of two shear bands which have initiated from the upper and lower specimen corners and propagated inside the shear zone. One can see that a crack started to propagate from the upper corner within the band whereas another crack, visible in the lower side of the picture, started to propagate along the band/matrix interface.

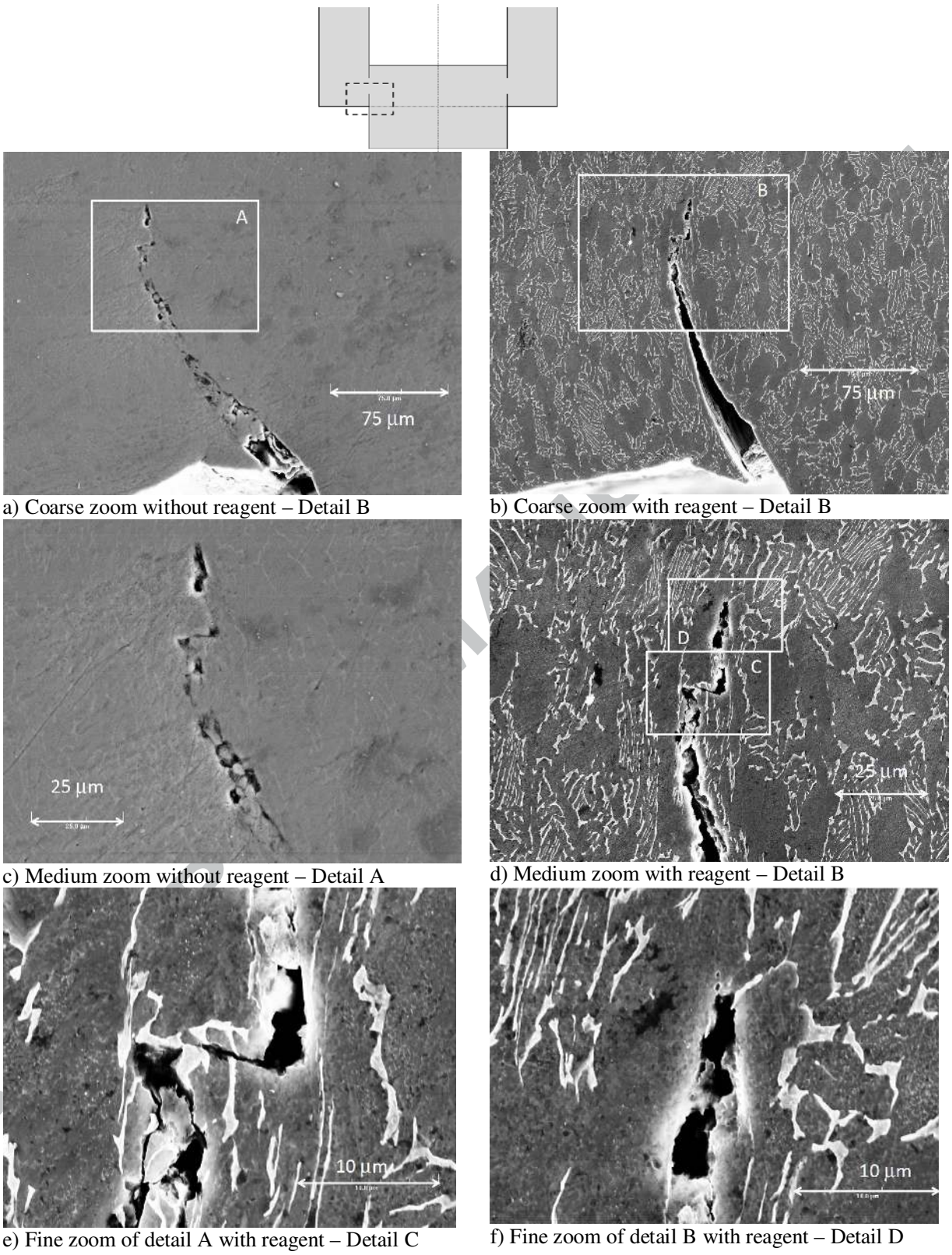

a) Coarse zoom without reagent – Detail B

b) Coarse zoom with reagent – Detail B

c) Medium zoom without reagent – Detail A

d) Medium zoom with reagent – Detail B

e) Fine zoom of detail A with reagent – Detail C

f) Fine zoom of detail B with reagent – Detail D

Fig.9: Partially fractured (Ma3) HSS-MM under interrupted shear-pressure loading at low strain rate, see also Longère and Dragon (2013). Averaged stress triaxiality close to -0.2. Ti-6Al-4V

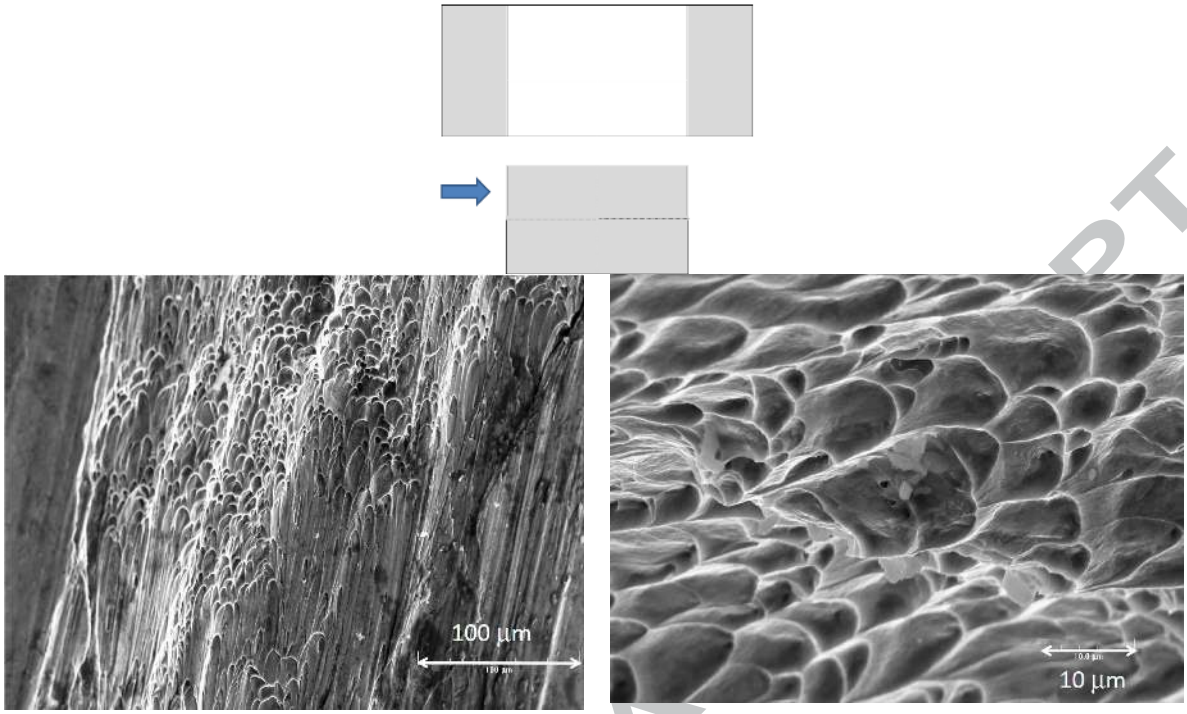

a) Dimple cluster surrounded by flat shear surfaces

b) Detail of a dimple cluster with inclusion containing dimples

Fig.10: Totally fractured (Ma1) HSS-MM under shear-pressure loading at low strain rate, see also Longère and Dragon (2013). Averaged stress triaxiality close to -0.2. Ti-6Al-4V

Fig.16 shows a crossing crack inside a totally fractured HSS-MM. Fig.16a shows that the overall compression loading leads ultimately to a (close to) 1 mm-(vertical) translation of the specimen left part wrt to the specimen right part (see the specimen, upper outer or lower inner corner). Thus the two (left and right) bulk parts visible in both Figs.16b and 16c do not match (they were not 'stuck' before the sample fracture) and have to be considered independently. In particular, the adiabatic shear bands crossing vertically both (left and right) bulk parts in Figs.16b-c are the same, the left one corresponding to a part of the unique ASB located 1 mm upper.

According to the detailed view in Fig.16b, see the specimen right bulk part, from the upper side to the lower side, the crack began to propagate inside the ASB, bifurcated on the left, propagated outside the band collinearly with the ASB direction, bifurcated once again but on the right this time, and then propagated outside the band collinearly with the ASB direction.

The ASB thickness is close to 10 µm, see Fig.16.c. In Fig.16.c, one can observe on both ASB sides a strong reorientation of the α' martensite needles (in white) in the direction of shearing. There remain only few tracks of these needles inside the ASB, as the result of a possible phase transformation – it has also been shown that a dynamic recrystallization operates during the ASB process, see e.g. Meyers et al. (1994) and Osovski et al. (2013).

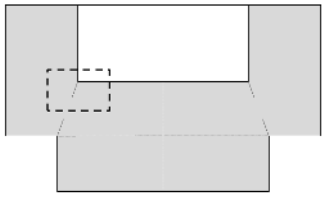

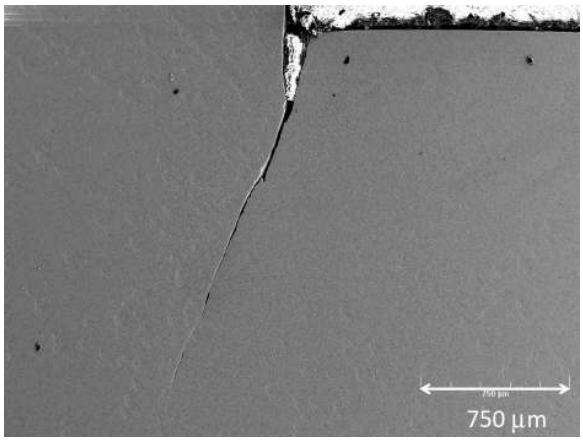

a) Coarse zoom without reagent

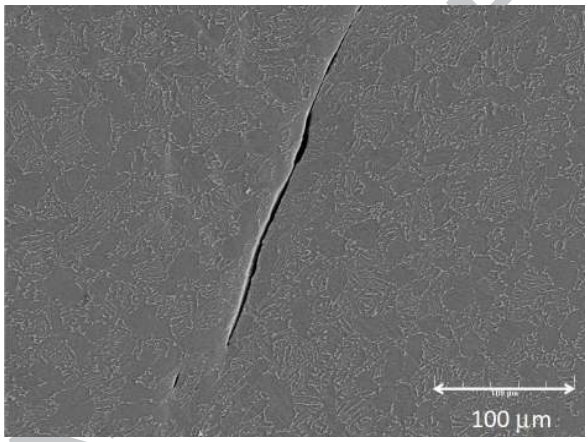

b) Medium zoom with reagent

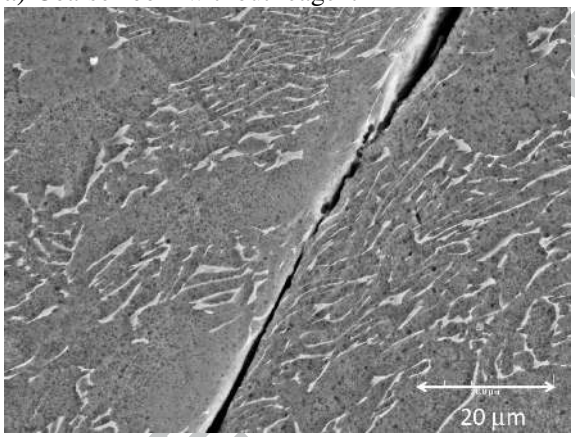

c) Fine zoom with reagent

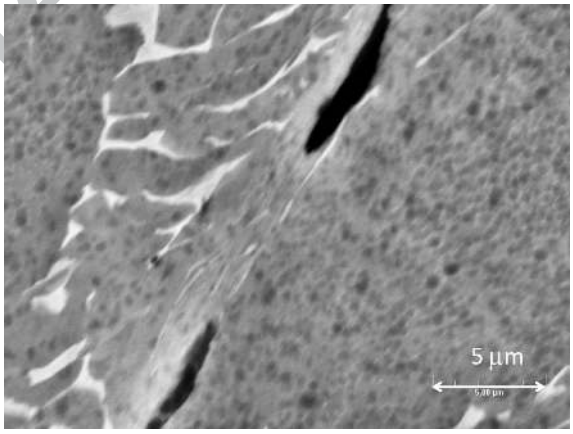

d) Very fine zoom with reagent

Fig.11: Partially fractured (Ca3) HSS-C under interrupted shear-pressure loading at low strain rate. Averaged stress triaxiality close to -0.5. Ti-6Al-4V

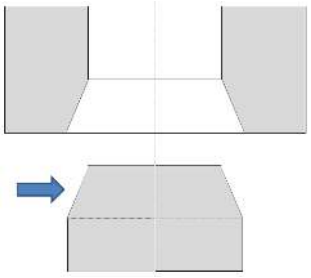

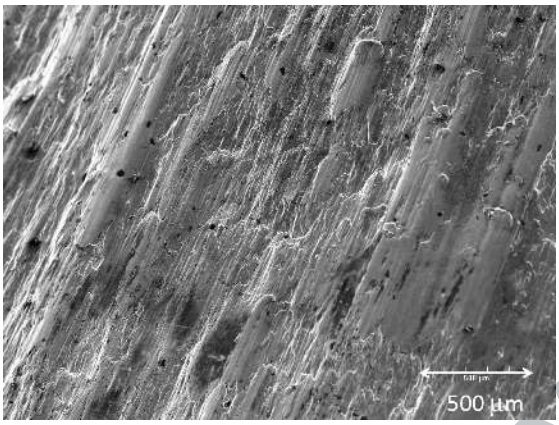

a) Corse zoom

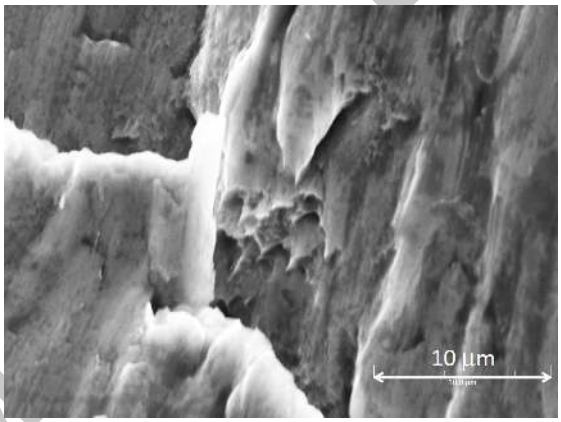

a) Fine zoom

Fig.12: Totally fractured (Ca1) HSS-C under shear-pressure loading at low strain rate. Averaged stress triaxiality close to -0.5. Ti-6Al-4V

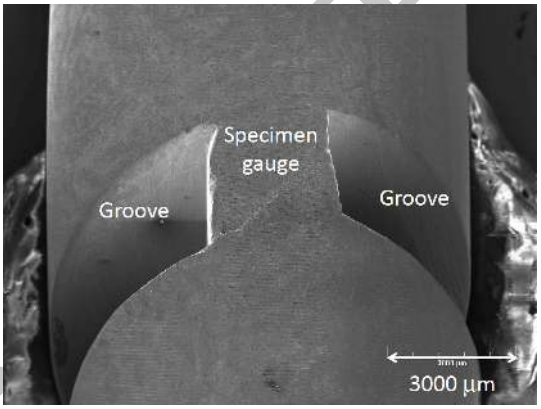

a) Coarse zoom

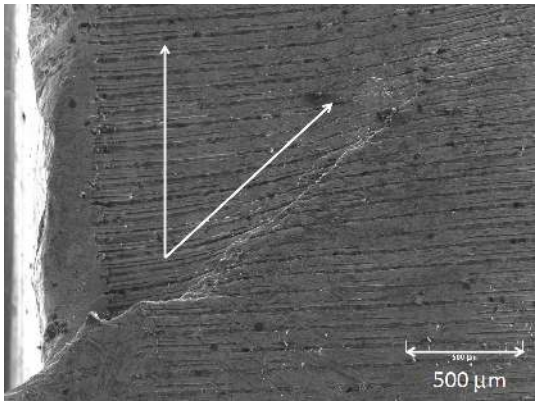

b) Medium zoom. The pattern of quasi horizontal lines corresponds with machining tracks. The crack is collinear with the inclined arrow.

Fig.13: Partially fractured (R3) SCS-RLR under interrupted shear-pressure loading at low strain rate. Averaged stress triaxiality close to -0.2. Ti-6Al-4V

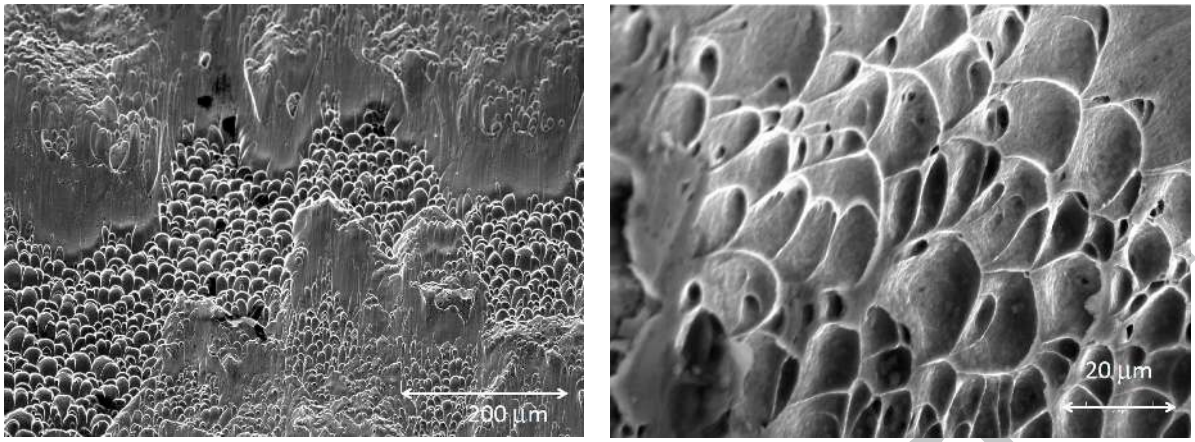

a) Coarse zoom b) Fine zoom

Fig.14: Totally fractured (R2) SCS-RLR under shear-pressure loading at low strain rate. Averaged stress triaxiality close to -0.2. Ti-6Al-4V

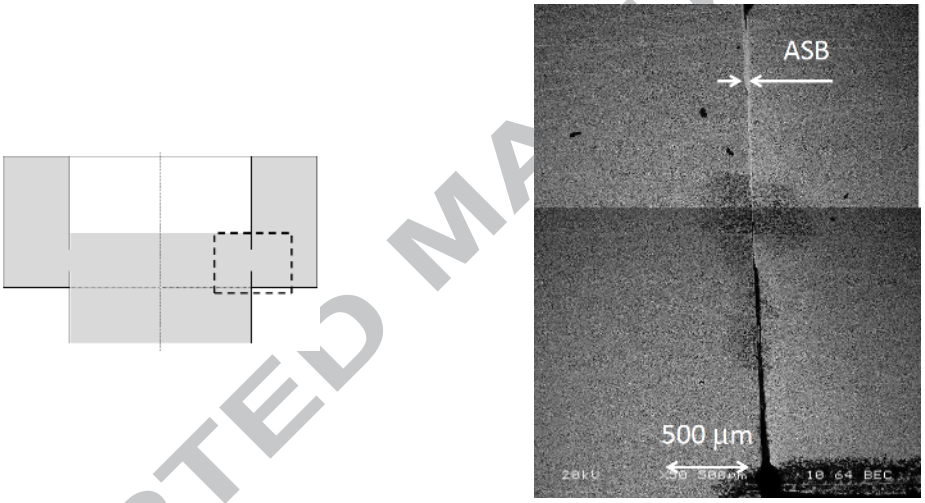

Fig.15: Partially fractured (Ma4) HSS-MM under interrupted shear-pressure loading at high strain rate. Averaged stress triaxiality close to -0.2. Ti-6Al-4V

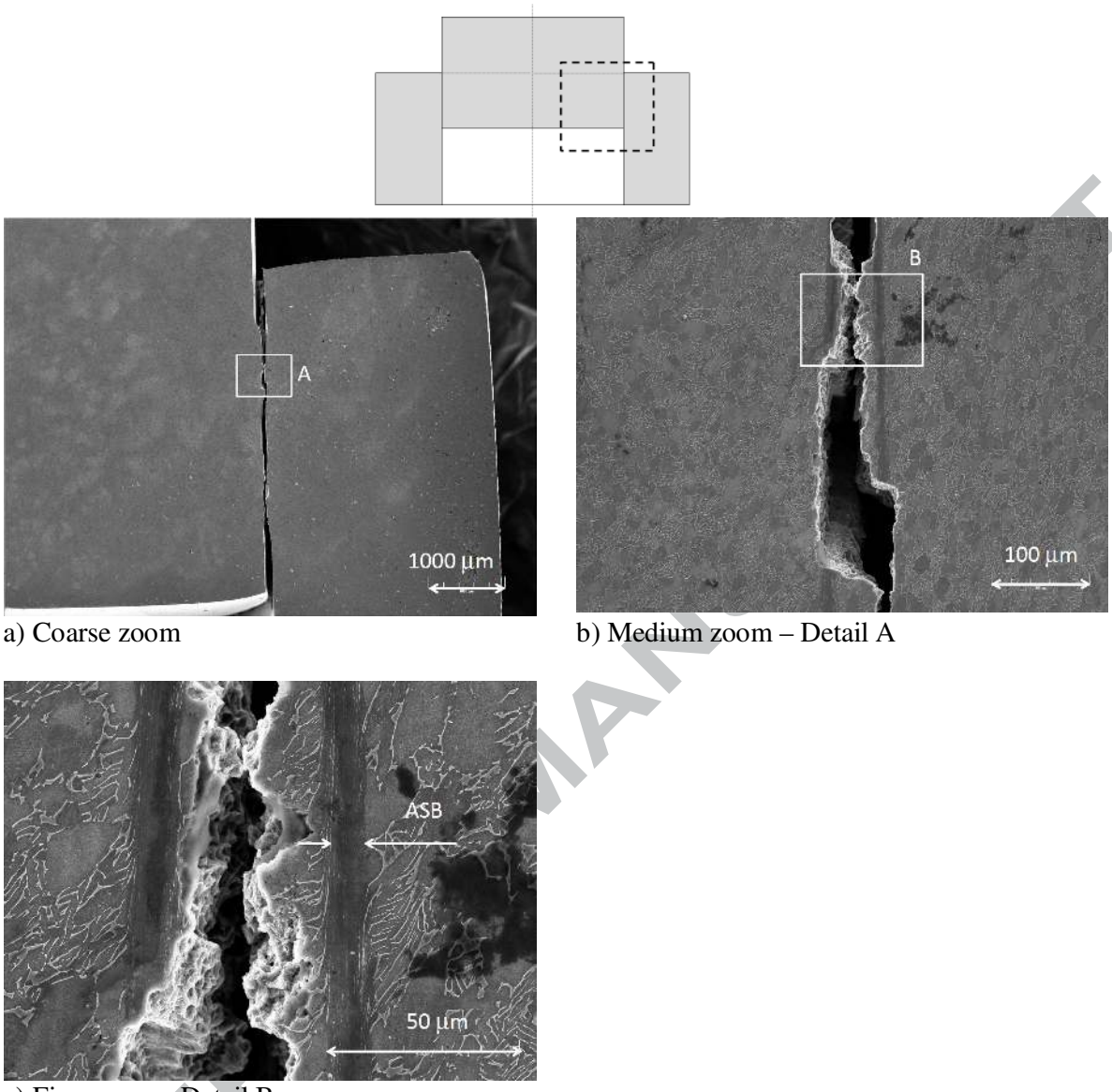

a) Coarse zoom

b) Medium zoom – Detail A

c) Fine zoom – Detail B

Fig.16: Totally fractured (Ma5) HSS-MM under shear-pressure loading at high strain rate. Averaged stress triaxiality close to -0.2. Ti-6Al-4V

Fig.17, showing a totally fractured SCS-RLR after a shear-compression test carried out until fracture, presents another experimental evidence of adiabatic shear banding as precursor of shear failure of Ti-6Al-4V under shear-pressure loading. The ASB thickness is here again close to 10 µm, and the crack propagated along the band/matrix interface with some crossings – not shown here. In the 3D views in Figs.17.b-c, one can clearly see that the ultimate fracture of the material at stake results from two successive steps: first adiabatic shear banding then void growth induced damage.

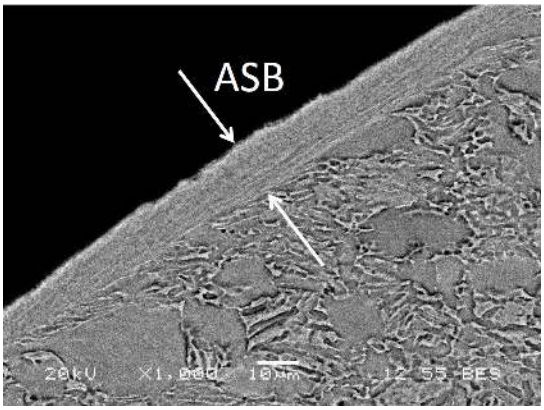

a) 2D view

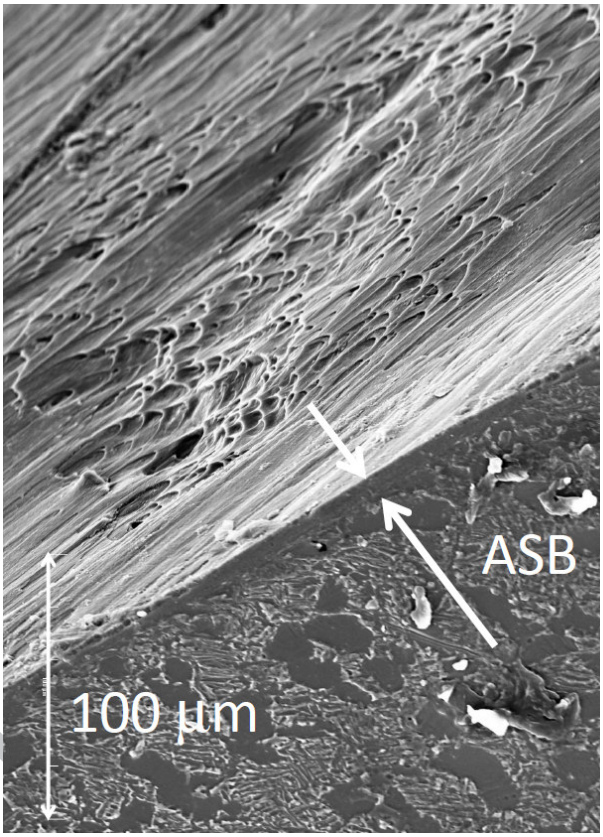

b) 3D view

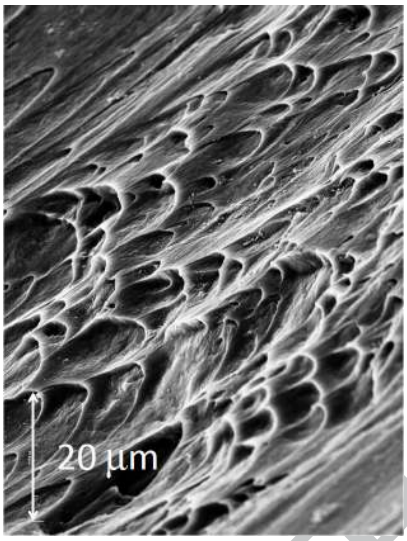

c) Detail of the 3D view fracture surface in b)

Fig.17: Totally fractured (R3) SCS-RLR under shear-pressure loading at moderate strain rate. Averaged stress triaxiality close to -0.2. Ti-6Al-4V

2.3.3. Low vs. moderate strain rate failure mechanisms

The experiments carried out in the present work at low and moderate strain rates allow to conclude that the fracture of Ti-6Al-4V titanium alloy under overall shear-pressure loading, involving stress triaxiality values ranging from -0.2 to -0.5, results from a void growth induced process. It is possible that during crack growth inside the sheared zone, currently under overall negative stress triaxiality loading, the stress state in the vicinity of the crack tip features a positive stress triaxiality as a consequence of particle-matrix or phase interface decohesion induced void germination and growth, which could explain the presence of dimples on the fracture surfaces.

In parallel, at moderate strain rate, due to the localization of the deformation within adiabatic shear bands, the failure of the material occurs earlier, leading to a shear strain at fracture smaller at moderate strain rate than at low strain rate. It has also been observed that, at low strain rate, the higher the pressure the larger the shear strain at failure.

3. Shear failure at high loading rate

In order to estimate the crack arrest ability of notched structures under dynamic conditions, Kalthoff and Winkler, see Kalthoff and Winkler (1987), proposed to impact the edge of double notched plates. They observed that below a critical velocity a crack propagates in (opening) Mode I at a significant angle (around +/-70°) wrt the notch plane and beyond this critical velocity the crack propagates in (ASB-assisted slipping) Mode II at a negligible (very slightly negative/positive) angle wrt the notch plane. In view of completing the experimental database on Ti-6Al-4V titanium alloy failure under impact loading, some results being obtained in this field by Zhou et al. (1996), we performed impact tests on KW-type double notched plates.

3.1. Experimental procedure

Impact tests were carried out using a 3m length- and 25 mm inner diameter-gas launcher. The projectile is a 25 mm length- and 20 mm diameter-steel cylinder settled in a 25 mm outer diameter foam cylinder. Ti-6Al-4V titanium alloy double notched plate dimensions are given in Fig.18.a. The 300µm height notches were machined by EDM (Electrical Discharge Machining), see Fig.18.b. A Photron RS3000 camera was used to observe the projectile/plate interaction at 75,000 fps and with a 128x128 pixel^2 spatial resolution.

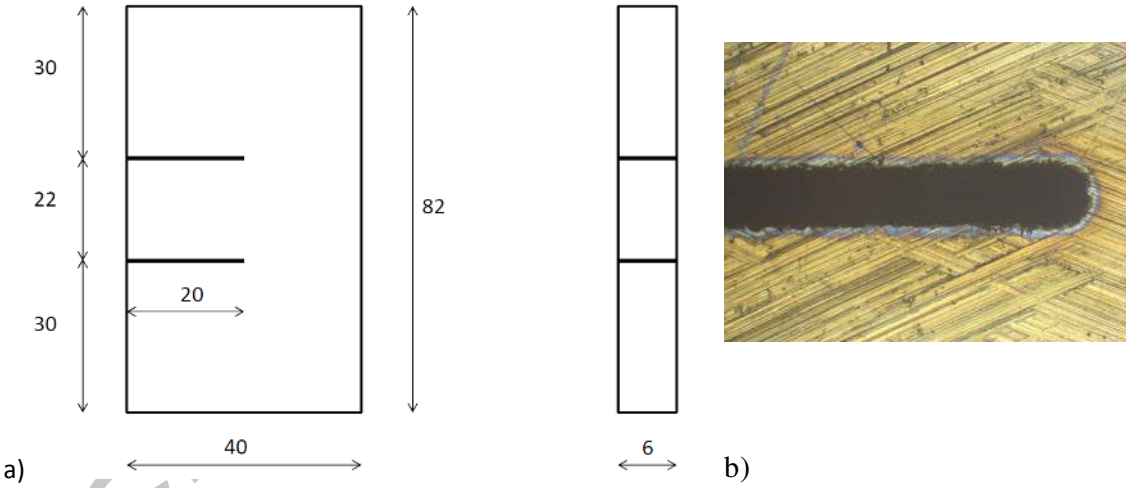

Fig.18: KW double notched plate. a) Dimensions. b) Detailed view of a 300µm height notch machined by EDM (inclined straight lines are milling tracks)

An example of sequence of frames obtained during the projectile/plate interaction with an impact velocity of 150 m/s is given in Fig.19. One can see an important light emission during this interaction, making difficult any accurate displacement field measurement – the symmetric curved cracks are however visible in bright white on frames b-d. For this reason, the comments in the following are only about a post-mortem plate.
The analysis of the impact test, carried out on a high strength steel (not shown here), from the high speed video recording shows a complex loading path. By analogy, we are briefly outlining the loading scenario deduced from this investigation to be possibly transposed to Ti-6Al-4V sample. It involves complex transient loading phenomena. For convenience, the

bulk part of the plate comprised between both notches is called impacted part and, accounting for the plate symmetries, discussion is about the upper half plate part only. The impact of the projectile onto the plate edge between the two notches generates a compression wave inside the impacted part. This compression wave has two main effects. The first effect, which is the expected one, is the transformation of the compression wave into a predominant shear wave at the notch tip, see Fig.20.b. Depending on the plate material dynamic toughness, a crack propagates or not from the notch tip. If the material is ductile enough, there is no crack propagation or at least the crack arrests inside the plate. The second effect, which is the unexpected one, is a direct consequence of the impacted part deformation. In the impacted part the compression wave indeed does not generate only a compression strain in the direction collinear with the impact axis but also a (Poisson effect induced) tension strain in the direction perpendicular to the impact axis. If the impact intensity is high enough, i.e. involving large tension strains, the notch lower lip happens to hit the notch upper lip. This generates a compression wave which propagates inside the plate upper part and reflected onto the plate upper free surface as a tension wave which in return propagates towards the notch and finally pulls the upper lip upwards, see Fig.20.c. This scenario may produce several times during the projectile/plate interaction, depending on the loading intensity and duration controlled by the projectile velocity and length, respectively. As a consequence, the notch/crack tip may be submitted to combined or alternating shear and tension loadings. This impact test is consequently a complex problem involving a complex loading sequence governed by wave propagations and interactions.

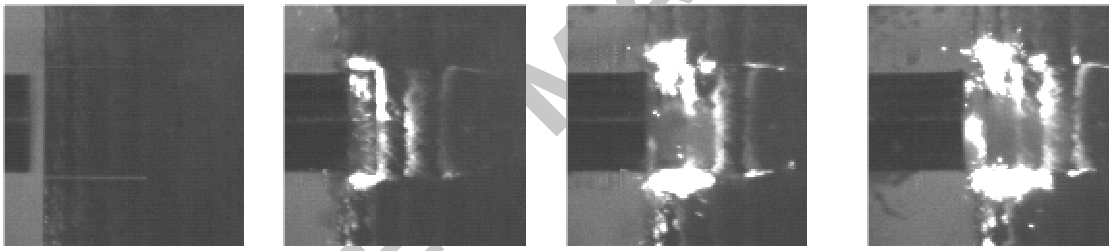

a) t_0 b) $t= t_0+67\mu s$ c) $t= t_0+133\mu s$ d) $t= t_0+200\mu s$

Fig.19: Sequence of frames during KW double notched plate impact loading Ti-6Al-4V

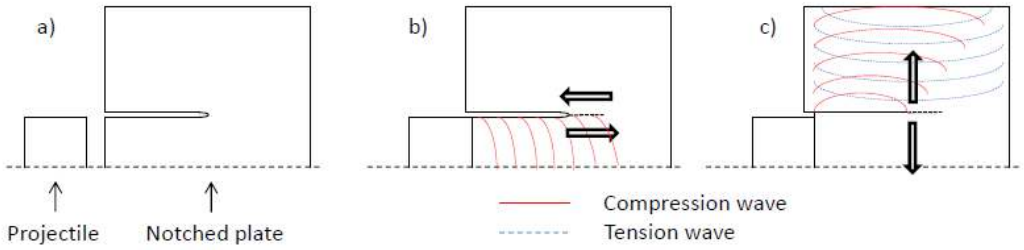

Fig.20: Schematic representation of possible wave propagation (uncoupled) effects during KW impact test. a) Configuration before impact accounting for plane symmetry. b) Shear wave induced Mode II crack propagation. c) Tension wave induced Mode I crack propagation. See comments above.

3.2. Fracture investigation

Impact tests at 106 m/s and 150 m/s were carried out on Ti-6Al-4V double notched plates. We are now analyzing the experimental results on the upper part of the plate. The impact at 106 m/s generated only a small (3 mm length) crack having propagated straight on from the notch. In the following the comments consequently focus on the much more interesting results obtained from the test performed at 150 m/s.

Fig.21 shows a curved crack which initiated from the notch tip and propagated inside the Ti-6Al-4V structure after the impact at 150 m/s. The crack length is close to 9 mm and the residual (i.e. after spring back) shear equivalent-CTOD is close to 600 µm. The crack may be coarsely split in two parts: the first part which is the longest covers almost all the crack length and is characterized by a curved propagation as shown in Figs.22.a-d ; the second part is the end of the crack and is characterized by a crack bifurcation, see Fig.22.e.

The initiation of the crack from the notch tip is characterized by elongated dimples, as shown in Fig.22.a. The very beginning of the crack growth consequently seems to proceed from predominant shearing induced Mode II crack propagation. Figs.22.b-d reveal the co-existence of zones of quasi spherical dimples and zones of elongated dimples, as the result of the superposition of alternating tension loading induced Mode I crack propagation on predominant shear loading induced Mode II crack propagation. Conversely, the crack bifurcation visible in Fig.22.d, characteristic of a change in the loading, seems to show that the tension loading, inducing Mode I crack propagation, became predominant. Finally, no adiabatic shear banding track has been found along the crack lip.

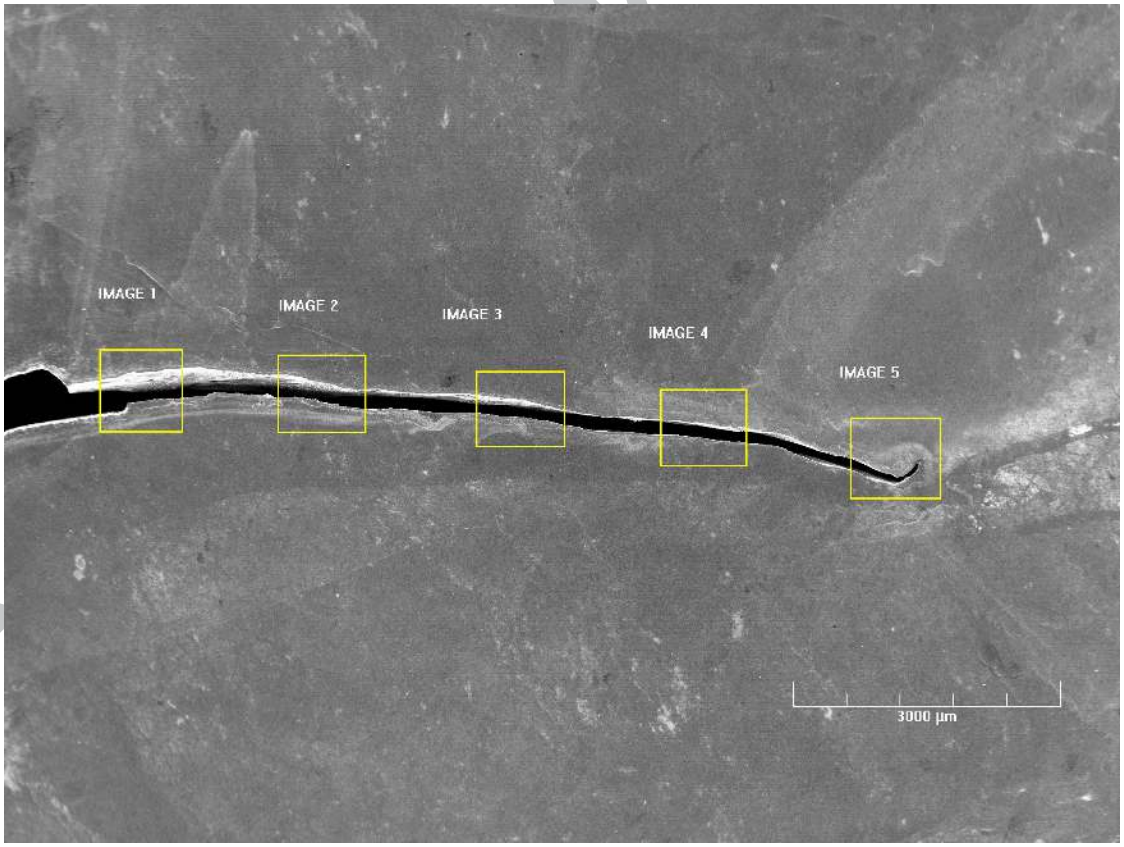

Fig.21: KW double notched plate after impact at 150 m/s – Macroscopic view after surface polishing - Ti-6Al-4V

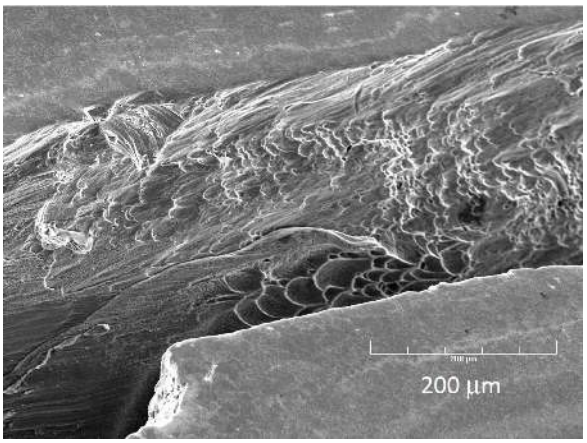

a) Image 1: evidence of elongated dimples near the notch tip

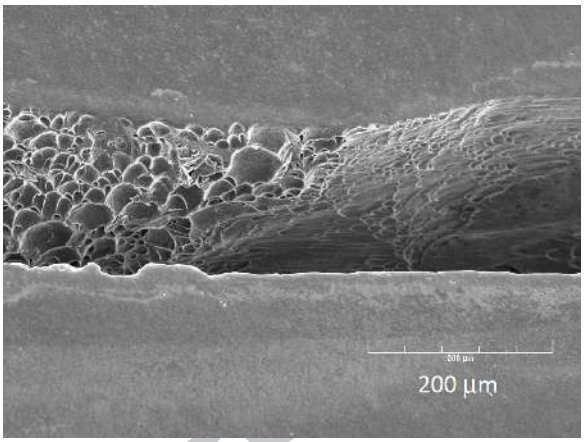

b) Image 2: coexistence of zones with quasi-spherical and elongated dimples

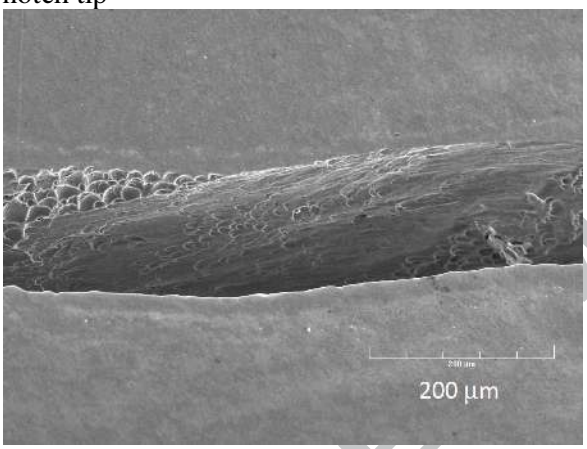

c) Image 3: flat surface separating zones with quasi-spherical dimples

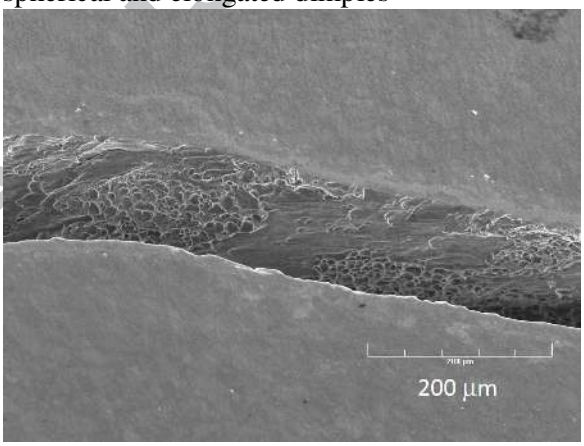

d) Image 4: see frame 3

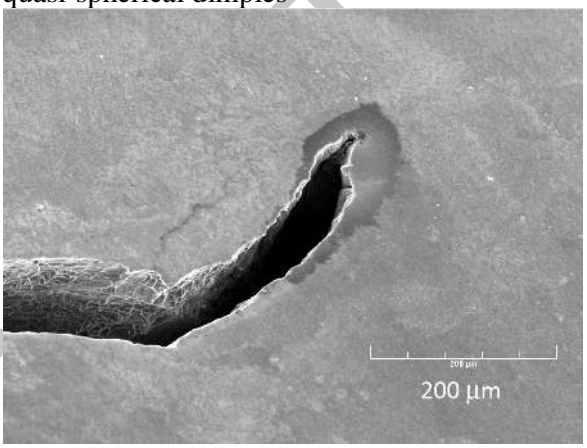

e) Image 5 - Crack bifurcation

Fig.22: KW double notched plate after impact at 150 m/s – Details of Fig.16
Ti-6Al-4V

The apparent disagreement between the latter result and the ASB controlled shear failure observed in impacted Ti-6Al-4V single notched plates by Zhou et al. (1996) can be

explained. The key point is probably the combination of the projectile kinetic energy and the specimen outer dimensions. In the present case, they are both lower than the ones used by the aforementioned authors. Increasing the kinetic energy allows generating higher strain rates and consequently favouring the conditions for ASB formation. On the other hand, increasing the specimen dimensions allows delaying the superposition of the reflected tension wave, see Fig.20.c, on the predominant shear wave, see Fig.20.b, keeping *de facto* a negative stress triaxiality state at the crack front, which also favours the conditions for adiabatic shear band development.

4. Concluding remarks

Starting from the observation of a lack of experimental results on the metal failure under overall shear-pressure loading, tests were carried out on Ti-6Al-4V shear-compression samples. The fracture investigation at the microstructure level concludes that the material failure under low and high strain rates results from a void growth induced process. However, at high strain rate, the localization of the deformation within adiabatic shear bands (which intervenes first in the failure process) creates conditions favorable for voiding, so that the failure of the material occurs earlier than at low strain rate. This leads to a shear strain at fracture smaller at high strain rate than at low strain rate. It must be noted that strain localization has also been observed as precursor (and not as a consequence) of ductile damage and further fracture in thin Al alloy sheet under positive stress triaxiality, see Morgeneyer et al. (2014).

In parallel, impact tests carried out on double notched plate edge showed that the interaction between tension and shear waves leads to a complex Mode I-Mode II crack propagation.
While remaining mainly qualitative, this experimental investigation is expected to be further used to discriminate constitutive models devoted to reproduce/predict metallic structures shear failure in a wide range of strain rates.

The complexity of mechanisms of deterioration and failure of Ti-6Al-4V accompanying moderate and dynamic deformation under shear-pressure low triaxiality loading conditions brings up again interactions and competition between the void growth ductile fracture phenomena and the adiabatic shearing related ones. The experimental evidence of coexistence of both events for high strain rates, impact loading related problems goes back possibly to 1980's. The review assessment by Woodward, see Woodward (1980), on material failure at high strain rates noticed firmly the fact of ductile fracture processes competing with adiabatic shear banding (ASB) and insisted on the necessity of deep metallurgical examination. It is stated in Woodward (1990) that the interaction/competition at stake occurs sometimes "with such a mix [that] it is not easy to interpret data in the terms of one mechanism only". Combined failure mechanisms have been notoriously observed and reported in dynamic mechanical testing reports on target failure by plugging. This fact has stimulated efforts to develop predictive models including thermomechanical approaches involving viscoplasticity and damage functions more or less coupled. Most of the models bring out a particular mechanism considered as predominant, e.g. spalling as in Davison et al. (1977) and Czarnota et al. (2008), ASB as in Nemat-Nasser et al. (1994) and Olsen et al. (1981). In the latter approach voids are considered as associated with shear band nucleation.

It is postulated thereby that a synthesis of models describing the material and kinematic consequences of void growth induced damage (Model I) and adiabatic shear banding induced degradation (Model II), as proposed by e.g. Longère and Dragon (2013) and

Longère et al. (2009), could lead to a tractable predictive 'unified' approach including the interaction/competition of the ductile fracture-void growth related mechanism and the ASB deterioration mechanism. These combined effects, experimentally evidenced for Ti-6Al-4V alloy in Sections 2 and 3 and recognized by the scientific and engineering community as frequently concomitant (see comments above) under negative/zero/small positive stress triaxiality, should be put forward in a composed framework capable to reproduce their interactions. Of course, no tractable models would result from superposition of the Models I and II cited above. A reasonable compromise is to be searched between conceptual pertinence and complexity of the unified approach and the tractability of the formalism, a number of material parameters to be identified, etc. Such a unified version including ASB vs ductile fracture interlocking will be presented in a forthcoming work.

Acknowledgment

The authors would like to thank DCNS Research for providing the material and DGA/MRIS (French Ministry of Defense) for its financial support, and acknowledge the contribution of O. Cherrier for some experiments.

References

Bai YL, Dodd B., 1992, Adiabatic shear localisation. Oxford: Pergamon Press.
Bai Y., Xue Q., Xu Y., Shen L., 1994, Characteristics and microstructure in the evolution of shear localization in Ti-6Al-4V alloy, Mech. Mat., 17, pp.155-164
Bao Y., Wierzbicki T., 2004, On fracture locus in the equivalent strain and stress triaxiality space, Int. J. Mech. Sci., 46, pp.81-98
Barsoum I., Faleskog J., 2007, Rupture mechanisms in combined tension and shear - Experiments, Int. J. Solids Struct., 44, pp.1768–1786
Beatty JH, Meyer LW, Meyers MA, Nemat-Nasser S., 1992, Formation of controlled adiabatic shear bands in AISI4340 high strength steel. In: Meyers MA, Murr LE, Staudhammer KP, editors. Shock-wave and high-strain-rate phenomena in materials. New York: Marcel Dekker, pp. 645–56.
Brünig M., Albrecht D., Gerke S., 2011. Modeling of ductile damage and fracture behavior based on different micromechanisms, Int. J. Damage Mech., 20, pp.558-577
Coppola T., Cortese L., Folgarait P., 2009, The effect of stress invariants on ductile fracture limit in steels, Eng. Fract. Mech., 76, pp.1288-1302
Couque H., 2003, A hydrodynamic hat specimen to investigate pressure and strain rate dependence on adiabatic shear band formation. J. Phys. IV, 110, pp.423–8
Czarnota C., Jacques N., Mercier S., Molinari A., 2008, Modelling of dynamic ductile fracture and application to the simulation of plate impact tests on tantalum, J. Mech. Phys. Solids, 56, pp.1624-1650
Davison L., Stevens A. L. and Kipp M. E., 1977, Theory of Spall Damage Accumulation in Ductile Metals, J. Mech. Phys. Solids, 25, pp. 11-28
Driemeier L., Brünig M., Micheli G., Alves M., 2010, Experiments on stress-triaxiality dependence of material behavior of aluminium alloys, Mech. Mat., 42, pp.207-217
Goods S.H., Brown L.M., 1979, The nucleation of cavities by plastic deformation, Acta. Metal., 27, pp.1-15
Hancock J.W.; Mackenzie A.C., 1976, On the mechanisms of ductile failure in high-strength steels subjected to multi-axial stress-states, J. Mech. Phys. Solids, 24, pp.147-169

Johnson G.R., Cook W.H., 1983, A constitutive model and data for metals subjected to large strains, high strain rates and high temperatures, in Proceedings of the Seventh International Symposium on Ballistics, The Hague, The Netherlands, pp.541-547.

Johnson G.R., Cook W.H., 1983, Fracture characteristics of three metals subjected to various strains, strain rates, temperatures and pressures. Engineering Fracture Mechanics 21(1), pp.31–48.

Kalthoff JF, Winkler S., 1987, Failure mode transition of high rates of shear loading. In: Chiem CY, Kunze H-D, Meyer LW, editors. Proceedings of the International Conference on Impact Loading and Dynamic Behavior of Materials, Germany: Deutsche Gesellschaft für Metallkunde, DGM-Verlag, Oberursel, pp.185–95.

Kalthoff JF, Bürgel A., 2004, Influence of loading rate on shear fracture toughness for failure mode transition, Int. J. Impact Eng., 30, pp.957-971

Liao SC., Duffy J., 1998, Adiabatic shear bands in Ti-6Al-4V alloy, J Mech Phys Solids, 46(11), pp.2201-2231

Longère P., Dragon A., Deprince X., 2009, Numerical study of impact penetration shearing employing finite strain viscoplasticity model incorporating adiabatic shear banding, J. Eng. Mat. Tech., ASME, 131, pp.011105.1-14

Longère P., Dragon A., 2013, Description of shear failure in ductile metals via back stress concept linked to damage-microporosity softening, Eng. Fract. Mech., 98, pp.92-108

Manach PY., Favier D., 1997, Shear and tensile thermomechanical behavior of near equiatomic NiTi alloy, Mat. Sci. Eng. A, 222, pp.45-57

Marchand A, Duffy J., 1988, An experimental study of the formation process of adiabatic shear bands in a structural steel, J Mech Phys Solids, 36(3), pp.251–83

Mazeau C, Beylat L, Longere P, Louvigné PF., 1997, On the quantitative evaluation of adiabatic shear banding sensitivity of various titanium alloys. J. Phys. IV, pp.429–34.

Meyer LW, Manwaring S. 1986, Critical adiabatic shear strength of low alloyed steel under compressive loading. In: Murr LE, Staudhammer KP, Meyers MA, editors. Metallurgical applications of shock-wave and high-strain-rate phenomena. New York: Marcel Dekker Inc., pp. 657–74

Meyers M.A., Subhash G., Kad. B.K., Prasad L., 1994, Evolution of microstructure and shear-band formation in α-hcp titanium, Mech. Mat., 17, pp.175-193

Mohr D, Oswald M., 2008, A new experimental technique for the multi-axial testing of advanced high strength steel sheets. Exp Mech, 48(1), pp.65–77.

Morgeneyer T.F., Taillandier-Thomas T., Helfen L., Baumbach T., Sinclair I., Roux S., Hild F., 2014, In situ 3-D observation of early strain localization during failure of thin Al alloy (2198) sheet, Acta Mater., 69, pp.78–91

Nemat-Nasser S., Li Y-F., Isaacs J.B., 1994, Experimental/computational evaluation of flow stress at high strain rates with applications to adiabatic shear banding, Mech. Mat., 17, pp. 111-134

Olsen G. B., Mescall J. F. and Azrin M., 1981, Adiabatic Deformation and Strain Localization,[in] Shock Waves and High Strain-Rate Phenomena in Metals (M. A. Meyers and L. E. Murr, Eds), Plenum, New York, pp. 221-247.

Osakada K., Watadani A., Sekiguchi H., 1977, Ductile fracture of Carbon steel under cold metal forming conditions (1st report, Tension and torsion tests under pressure), Bulletin of the JSME, 20, 150, pp.1557-1565

Osovski S., Rittel D., Venkert A., 2013, The respective influence of microstructural and thermal softening on adiabatic shear localization, Mech. Mat., 56, pp.11-22

Papasidero J., Doquet V., Mohr D., 2013, Determination of the effect of stress state on the onset of ductile fracture through tension-torsion experiments, to be published in Exp. Mech.

Rittel D., Lee S., Ravichandran G., 2002, A shear-compression specimen for large strain testing, Exp. Mech., 42, pp.58-64

Vural M., Rittel D., Ravichandran G., 2003, Large strain mechanical behavior of 1018 cold-rolled steel over a wide range of strain rates, Metal. Mat. Trans. A, 34A, pp.2873-2885

Woodward R.L., 1990, Material failure at high strain rates, in High velocity impact dynamics, ed. by J.A. Zukas, John Wiley & Sons, pp.65-125

Zhou M., Rosakis A.J., Ravichandran G., 1996, Dynamically propagating shear bands in impact-loaded prenotched plates-I. Experimental investigations of temperature signatures and propagation speed, J. Mech. Phys. Solids, 44 (6), pp.981-1006.